denoting transitions from the upper to the lower atomic state. This total spontaneous emission can be decomposed, without changing equation (7), into parts $C_1 = C_2 = \sqrt{\Phi\Gamma}\sigma^-$ and $C_3 = \sqrt{(1-2\Phi)\Gamma}\sigma^-$, which stand for spontaneous emission in the direction of the detector, in the opposite direction (towards the mirror), and in the remaining solid angle, respectively. The action of the mirror is now described by replacing C_1 and C_2 in equation (7) by the coherent sum

$$C_{12} = C_1 + e^{-i\omega_l\tau}C_2 = \sqrt{\Phi\Gamma}(1 + e^{-i\omega_l\tau})\sigma^- \quad (8)$$

with laser frequency ω_l, and Φ denoting the effective fraction of the total fluorescence which can be brought to interference, including the contrast reduction by atomic motion, by $g^{(1)}$, and by wavefront distortions. Equation (8) models precisely the situation where the decay that the detector observes is the superposition of the two possible directions, one being delayed by τ. An OBE calculation with this modified dissipation predicts a variation of the total fluorescence with the ion–mirror distance at a level determined by Φ. This is inhibited and enhanced spontaneous emission; it can also be regarded as resulting from reabsorption or stimulated emission induced by the back-reflected photons.

In the two-ion case, the two indistinguishable processes which interfere are emission by one ion towards the detector and emission by the other ion towards the mirror. Using the same tools as above, we model the situation by adding coherently the two decay processes C_{a1} and C_{b2} (and vice versa) where now a and b label the ions and 1 and 2 label the directions of emission. The two new decay operators are given by

$$C_{ab} = C_{a1} + e^{-i\omega_l\tau}C_{b2};\ \ C_{ba} = C_{b1} + e^{-i\omega_l\tau}C_{a2}. \quad (9)$$

When these are introduced into equation (7) (now ρ is the two-atom density matrix), then a term $(\sigma_a^+\sigma_b^- + \sigma_b^+\sigma_a^-)\cos(\omega_l\tau)\rho$ appears in the OBEs, which describes simultaneous emission by one ion and absorption by the other and which is modulated with the distance between the ions via the mirror. This shows that in fact reabsorption (and its inhibition) of the emitted photons goes along with the observed interference. A slightly different viewpoint is that, depending on the phase factor $e^{i\omega_l\tau}$, either the symmetric or the antisymmetric two-atom wave function is preferentially populated, which leads to enhanced or suppressed collective spontaneous emission, respectively. This is subradiance and superradiance as originally described by Dicke[13].

Received 28 March; accepted 25 July 2001.

1. Purcell, E. M. Spontaneous emission probabilities at radio frequencies. *Phys. Rev.* **69,** 681 (1946).
2. Milonni, P. W. *The Quantum Vacuum* Ch. 6 (Academic, San Diego, 1994).
3. Drexhage, K. H. in *Progress in Optics* (ed. Wolf, E.) Vol. 12, 163–232 (North-Holland, Amsterdam, 1974).
4. DeMartini, F., Innocenti, G., Jacobovitz, G. R. & Mataloni, P. Anomalous spontaneous emission time in a microscopic optical cavity. *Phys. Rev. Lett.* **59,** 2955–2958 (1987).
5. Jhe, W. *et al.* Suppression of spontaneous decay at optical frequencies: Test of vacuum-field anisotropy in confined space. *Phys. Rev. Lett.* **58,** 666–669 (1987).
6. Heinzen, D. J., Childs, J. J., Thomas, J. F. & Feld, M. S. Enhanced and inhibited visible spontaneous emission by atoms in a confocal resonator. *Phys. Rev. Lett.* **58,** 1320–1323 (1987).
7. Hood, C. J., Lynn, T. W., Doherty, A. C., Parkins, A. S. & Kimble, H. J. The atom-cavity microscope: Single atoms bound in orbit by single photons. *Science* **287,** 1447–1453 (2000).
8. Pinkse, P. W. H., Fischer, T., Maunz, P. & Rempe, G. Trapping an atom with single photons. *Nature* **404,** 365–368 (2000).
9. Goy, P., Raimond, J. M., Gross, M. & Haroche, S. Observation of cavity-enhanced single-atom spontaneous emission. *Phys. Rev. Lett.* **50,** 1903–1906 (1983).
10. Hulet, R. G., Hilfer, E. S. & Kleppner, D. Inhibited spontaneous emission by a Rydberg atom. *Phys. Rev. Lett.* **55,** 2137–2140 (1985).
11. Rempe, G., Walther, H. & Klein, N. Observation of quantum collapse and revival in a one-atom maser. *Phys. Rev. Lett.* **58,** 353–356 (1987).
12. Gabrielse, G. & Dehmelt, H. G. Observation of inhibited spontaneous emission. *Phys. Rev. Lett.* **55,** 67–70 (1985).
13. Dicke, R. H. Coherence in spontaneous radiation processes. *Phys. Rev.* **93,** 99–110 (1954).
14. DeVoe, R. G. & Brewer, R. G. Observation of superradiant and subradiant spontaneous emission of two trapped ions. *Phys. Rev. Lett.* **76,** 2049–2052 (1996).
15. Nagourney, W., Sandberg, J. & Dehmelt, H. Shelved optical electron amplifier: Observation of quantum jumps. *Phys. Rev. Lett.* **56,** 2797–2799 (1986).
16. Sauter, Th., Neuhauser, W., Blatt, R. & Toschek, P. E. Observation of quantum jumps. *Phys. Rev. Lett.* **57,** 1696–1698 (1986).
17. Bergquist, J. C., Hulet, R. G., Itano, W. M. & Wineland, D. J. Observation of quantum jumps in a single atom. *Phys. Rev. Lett.* **57,** 1699–1702 (1986).
18. Diedrich, F. & Walther, H. Nonclassical radiation of a single stored ion. *Phys. Rev. Lett.* **58,** 203–206 (1987).
19. Sackett, C. A. *et al.* Experimental entanglement of four particles. *Nature* **404,** 256–259 (2000).
20. Moerner, W. E. in *Atomic Physics 14* (eds Wineland, D. J., Wieman, C. E. & Smith, S. J.) AIP Conf. Proc. Vol. 323, 467–486 (AIP Press, New York, 1995).
21. Loudon, R. *The Quantum Theory of Light* (Oxford Univ. Press, Oxford, 1983).
22. Raab, C. *et al.* Diode laser spectrometer at 493 nm for single trapped Ba^+ ions. *Appl. Phys. B* **67,** 683–688 (1998); *Appl. Phys. B* **69,** 253 (1999).
23. Raab, C. *et al.* Motional sidebands and direct measurement of the cooling rate in the resonance fluorescence of a single trapped ion. *Phys. Rev. Lett.* **85,** 538–541 (2000).
24. Schubert, M., Siemers, I., Blatt, R., Neuhauser, W. & Toschek, P. E. Transient internal dynamics of a multilevel ion. *Phys. Rev. A* **52,** 2994–3006 (1995).

Acknowledgements

We thank P. Zoller, D. Leibfried and G. Morigi for helpful discussions. We gratefully acknowledge support by the European Commission (TMR network QSTRUCT), by the Austrian Science Fund (FWF), and by the Institut für Quanteninformation GmbH.

Correspondence and requests for materials should be addressed to J.E. (e-mail: juergen.eschner@uibk.ac.at).

Bose–Einstein condensation on a microelectronic chip

W. Hänsel, P. Hommelhoff, T. W. Hänsch & J. Reichel

Max-Planck-Institut für Quantenoptik and Sektion Physik der Ludwig-Maximilians-Universität, Schellingstr. 4, D-80799 München, Germany

Although Bose–Einstein condensates[1–3] of ultracold atoms have been experimentally realizable for several years, their formation and manipulation still impose considerable technical challenges. An all-optical technique[4] that enables faster production of Bose–Einstein condensates was recently reported. Here we demonstrate that the formation of a condensate can be greatly simplified using a microscopic magnetic trap on a chip[5]. We achieve Bose–Einstein condensation inside the single vapour cell of a magneto-optical trap in as little as 700 ms—more than a factor of ten faster than typical experiments, and a factor of three faster than the all-optical technique[4]. A coherent matter wave is emitted normal to the chip surface when the trapped atoms are released into free fall; alternatively, we couple the condensate into an 'atomic conveyor belt'[6], which is used to transport the condensed cloud non-destructively over a macroscopic distance parallel to the chip surface. The possibility of manipulating laser-like coherent matter waves with such an integrated atom-optical system holds promise for applications in interferometry, holography, microscopy, atom lithography and quantum information processing[7].

Some of the advantages of microscopic magnetic traps on a chip have been pointed out before. Modest electric currents can produce large magnetic field gradients and curvatures in close proximity to a planar arrangement of wires[8]. In an experiment which was realized simultaneously with the results reported here, microfabricated parallel conductors were used in a last stage of evaporative cooling to achieve Bose–Einstein condensation (BEC)[9]. Lithographic fabrication techniques now make it possible to integrate even complex systems of many microscopic traps, waveguides[10,11], and other atom-optical devices[12–14] on a single 'atom chip'.

The use of such microtraps for BEC appears, in hindsight, only natural, as quantum-mechanical phenomena tend to be more readily observable on a smaller scale. A tight trap permits fast adiabatic changes of the confining potential, and it becomes easy to magnetically compress a trapped atom cloud so that elastic collision times of the order of milliseconds are reached even with just a few million trapped atoms. The resulting fast thermalization makes it possible to drastically shorten the time for radio-frequency-assisted evaporative cooling[15]. It is also advantageous that a tight magnetic confinement positions the atom cloud near the centre of the magnetic trap, despite the pull of gravity, so that a rather uniform evaporation is achieved throughout the evaporation process. Collisions with background gas atoms become less important during such a fast cooling cycle, so that the previously very stringent requirements on the vacuum may be greatly relaxed.

Figure 1a shows the chip that is used in our BEC experiments. It features 50-μm-wide conductors, which reproducibly support continuous currents in excess of 3 A. The chip was fabricated

using thin-film hybrid technology, a standard microelectronics process[14]. Although a variety of fabrication techniques can be used (several groups have developed custom processes[16,25]), a standard process has the advantage of being available to non-microtechnology laboratories.

In our chip traps, the trapping potential is produced by superposing the field of the lithographic conductors with a homogeneous, external bias field $\mathbf{B}_0$. A Ioffe–Pritchard potential (non-zero field in the minimum, and quadratic dependence close to this minimum) is created using the 'Z'-shaped conductor shown in yellow in Fig. 1a; the central part of this conductor has a length of 1.95 mm. Figure 1b shows the magnetic potentials created by this wire with a current of $I_0 = 2$ A for two different values of the external bias field, $\mathbf{B}_0 = B_x\mathbf{e}_x + B_y\mathbf{e}_y$ (where $\mathbf{e}_x$ and $\mathbf{e}_y$ are unit vectors): ($B_x = 0$, $B_y = 8$ G) and ($B_x = 1.9$ G, $B_y = 55$ G), corresponding to the two extreme values used in the experiment. With increasing bias field, the trap centre moves closer to the surface, from $z_0 = 445\,\mu$m to $z_0 = 70\,\mu$m. The potentials vary quadratically with the distance from the trap centre for very small distances. In the main part of the trap, the transverse dependence can be approximately characterized by the gradient of the wire field at z_0. This gradient rises by a factor of 37—from 200 G cm^{-1} to 7,300 G cm^{-1}—for the two potentials in the figure. The central part of the longitudinal potential, on the other hand, changes very little while its steep walls grow higher with trap compression.

The chip that creates these potentials is mounted face down in a glass cell of inner dimensions 30 × 30 × 110 mm; this cell is part of a simple vacuum system pumped by a 25 l s^{-1} ion pump and a small titanium sublimator (Fig. 2). The magnetic trap lifetime is up to 5 s, which indicates a background pressure in the 10^{-9} mbar range. Thermal rubidium vapour is produced from a rubidium dispenser[17]. We operate it at low, constant, current, so that the rubidium partial pressure remains low and reduces the magnetic trap lifetime by less than 20%. During the magneto-optical trap (MOT) loading phase, a 30-W halogen reflector bulb is switched on to temporarily increase the rubidium pressure by light-induced desorption[18]. The MOT loaded in this way contains about 5×10^6 atoms of ^{87}Rb after a loading time of 3–7 s.

Trap loading is a crucial step in realizing a magnetic microtrap. We use the mirror-MOT technique developed in our group and described in detail in refs 5 and 14. This variant of the well-known MOT provides a sample of laser-cooled atoms at a distance of less than 1 mm from the substrate surface, and enables *in situ* transfer into the magnetic microtrap without requiring an intermediate, macroscopic magnetic trap. In this way we typically load 3×10^6 atoms into the magnetic trap after optical pumping into the $F = 2$, $m_F = 2$ ground state.

The initial magnetic trapping potential is shown in dashed lines in Fig. 1b. This trap has frequencies $\nu_x = 28$ Hz and $\nu_{y,z} = 220$ Hz. The temperature and peak density, measured 200 ms after transfer from the MOT, are ~45 μK and ~5×10^{10} cm^{-3}, respectively. Immediately after the transfer, we increase the bias field B_y in 300 ms to a final value of 55 G, leading to the potential shown in solid lines in Fig. 1b. Thus, strong compression occurs in the transverse (y, z) plane, whereas the longitudinal potential undergoes a comparatively small change. The very anisotropic final potential has a transverse curvature of 2.4×10^7 G cm^{-2} near the centre, leading to a calculated transverse oscillation frequency of $\nu_{y,z} = 6.2$ kHz, while the longitudinal frequency is only $\nu_x = 17$ Hz. Experimentally, we have used two different techniques (direct observation of the oscillation and parametric heating) to measure these frequencies, and found good agreement of calculated and measured frequencies.

Immediately after compression, we initiate forced evaporative cooling with a linear radio-frequency sweep from 30 MHz to 8 MHz. This sweep is typically performed in 900 ms, and reduces the number of atoms to 5×10^5. From here, we can proceed to BEC by two different routes, both of which involve an adiabatic change in the potential. In the first case, the trap is simply decompressed by reducing $\mathbf{B}_0$—leading to a very elongated condensate centred at the position C1 in Fig. 1a. In the second approach, the wire currents are

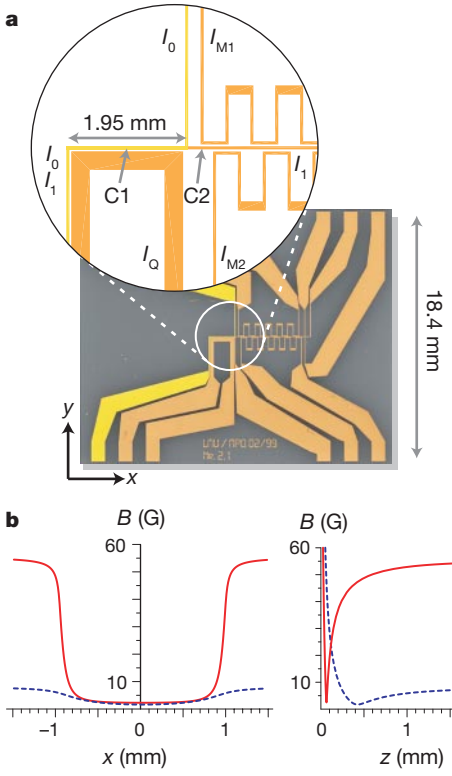

Figure 1 The chip and the magnetic potentials that it creates. **a**, Layout of the lithographic gold wires on the substrate. The inset shows the relevant part of the conductor pattern. I_0, I_1, I_{M1} and I_{M2} create the various magnetic potentials for trapping (see **b**) and transport, as described in the main text, I_0 is used only during trap loading (intermediate MOT step[5]). **b**, Potentials created by a wire current $I_0 = 2$ A for two different values of the external bias field, ($B_x = 0$, $B_y = 8$ G) (dashed lines) and ($B_x = 1.9$ G, $B_y = 55$ G) (solid lines).

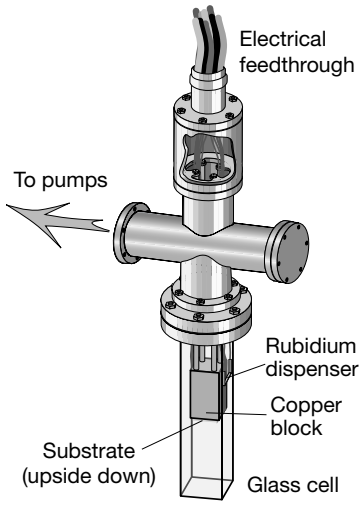

Figure 2 Vacuum system. Because of the efficient evaporation in the chip trap, this very simple set-up is sufficient to achieve Bose–Einstein condensation (BEC). The substrate is mounted facing downwards, so that the atom cloud may be released to expand in free fall (time-of-flight analysis).

also modified to move the trap centre to position C2, where a more spherical condensate arises.

We now describe both cases in more detail. In the first case, the initial radio-frequency ramp is immediately followed by a second, exponential ramp with 800 ms duration. At the end of this ramp, $\sim 7 \times 10^4$ atoms are left at a temperature of $\sim 6\,\mu$K, a density of 5×10^{13} cm^{-3} and a phase space density in the lower 10^{-2} range. The external bias field is now reduced to ($B_x = 1.2$ G, $B_y = 40$ G) within 150 ms to decompress the trap. This is done to avoid an excessively high density (which would lead to trap loss by three-body collisions), and to reduce the heating rate, which was measured to be 2.7 μK s^{-1} in the compressed trap at $B_y = 55$ G, and reduced to 1.1 μK s^{-1} at $B_y = 40$ G. (The origin of this heating is discussed below.) The decompressed trap has frequencies $\nu_{x,y,z} = (20, 3{,}900, 3{,}900)$ Hz. After a final radio-frequency sweep to $\sim$1.6 MHz in 300 ms, a condensate appears. Figure 3 shows time-of-flight absorption images after a ballistic expansion time of 21 ms. These images were taken for descending values of the final radio frequency, and show the appearance of the sharp, non-isotropic peak in the momentum distribution which is a key signature of BEC. A bimodal distribution is first observed for a temperature of $T \approx 630$ nK, in agreement with the theoretical value of the transition temperature $T_c = 670$ nK (for 11,000 atoms). The condensate lifetime is of the order of 500 ms and can be prolonged to $\sim$1.3 s when the radio-frequency power is left on at a frequency just above resonance with the condensed atoms. The number of condensate atoms in a distribution well below the transition temperature is typically around 3,000.

The high trap frequencies in the compressed traps currently prevent us from measuring directly the temperature and density in these traps. Instead, we infer these values from analysing the cloud after adiabatic decompression, using a bias field B_y of 19.4 G for the elongated trap, and of 16 G for configuration C2. Detection can then be accomplished by shutting off the wire current, leaving the homogeneous field switched on and tuning the probe laser frequency to the Zeeman-shifted atomic resonance. If the atom cloud is cold enough to remain in the quadratic region of the potential, the temperature in the compressed trap can be calculated from the relation $T' = (\nu_1'\nu_2'\nu_3'/(\nu_1\nu_2\nu_3))^{1/3}T$, where ν_i indicates a trap frequency along the i-th axis, and ν_i' designates a value after the transformation. The temperatures we cite are inferred in this way, with the exception of the heating rate measurements below, where all values are given for the detection trap, so that they can be compared directly.

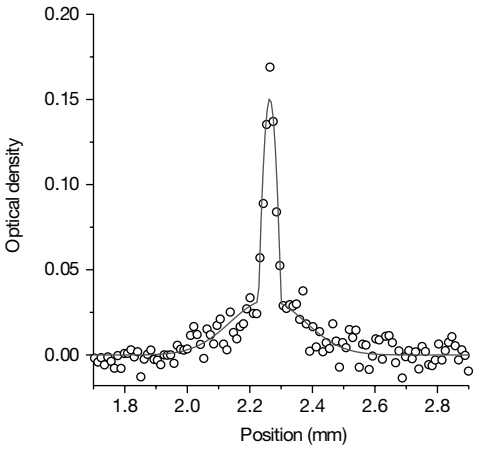

Figure 4 Axial column density profile near the transition temperature, taken in configuration C2. The curve is obtained from a two-dimensional best fit to a bimodal distribution, which corresponds to 1,600 atoms in the condensate and 10,400 atoms in the thermal component at a temperature of 1.7 μK.

Owing to its very elongated shape, the condensate in position C1 is well inside the regime of fluctuating phase. Such 'quasicondensates' are at present receiving much attention[19,20]. We also reach the phase transition in a more spherical configuration by transferring the cloud to the position marked C2 in Fig. 1a. This is accomplished by ramping the currents and external fields to final values $I_1 = 2$ A, $I_{M1} = 1$ A, $B_x = 5$ G and $B_y = 40$ G. This transformation takes 250 ms, and results in a trap with frequencies $\nu_{x,y,z} = (300, 3{,}400, 3{,}500)$ Hz—the ratio of transverse and longitudinal frequencies is now only 12:1, in contrast to configuration C1, where it was 200:1. A single additional radio-frequency ramp with a duration of 500 ms and a final frequency of $\sim$1.0 MHz is enough to achieve condensation in this trap. The number of

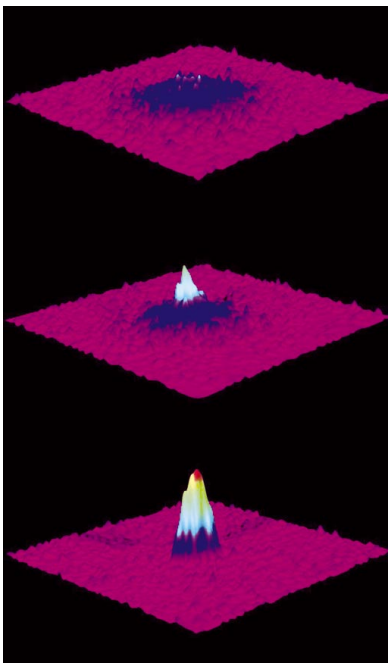

Figure 3 Time-of-flight absorption images of the atom cloud after 21 ms of free expansion. (Profile height and false colours are used to encode the optical density of the cloud.) The images were taken after a final radio-frequency sweep ending at frequencies $\nu_s = \nu_0 + 66$ kHz, 44 kHz and 15 kHz (from top to bottom), where ν_0 is the resonance frequency in the centre of the trap. The images show the appearance of the sharp, non-isotropic peak in the momentum distribution which is a key signature of BEC.

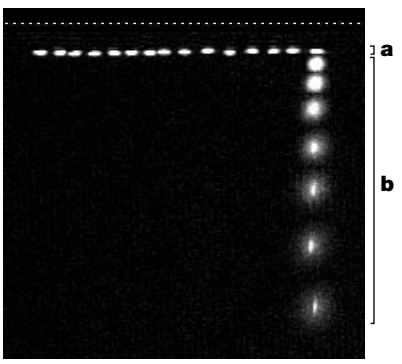

Figure 5 Transport of a BEC on the 'magnetic conveyor belt'. **a**, Superposed absorption images taken at fixed time intervals during transport. The distance between the first and last image is 1.6 mm, the transport time is 100 ms. The line of sight is parallel to the y axis (see Fig. 1); the dotted line marks the edge of the substrate. **b**, Time-of-flight images of the atom cloud after release at the final position, exhibiting the bimodal structure characteristic of a BEC. The maximum expansion time (bottom image) is 19.3 ms.

condensed atoms is typically slightly higher than in configuration C1. A section through a condensed cloud, taken close to the condensation threshold (Fig. 4), reveals the expected bimodal structure with a broad gaussian background of thermal atoms and a sharp peak due to the condensed fraction. When using this potential, we even observe condensation when both radio-frequency ramps are shortened and overlapped with the magnetic field ramp, so that the total evaporation time is as short as 700 ms.

The short evaporation time entails a very fast cycle time of 10 s or less, including MOT loading and detection. Moreover, it relaxes the ultrahigh-vacuum requirements that have been one of the main restrictions of 'traditional' BEC experiments, and thus enables us to use the very simple vacuum system of Fig. 2.

With its trap–substrate distance in the 100-μm range, the microtrapped condensate approaches a room-temperature surface much more closely than do usual condensates. Little is known about condensate–surface interactions at very small distances. Surface-induced heating of trapped atom clouds has been studied theoretically[21], and is predicted to become important for distances in the 10-μm range. However, there are many other sources that could explain our observed heating rate, such as electrical current noise, mechanical vibrations, and various effects associated with collisions[22]. We have measured the heating rate after slowly reducing both I_0 and B_y by the same factor α, starting from $I_0 = 2$ A, $B_y = 40$ G. This operation reduces both the transverse and longitudinal gradients and curvatures by α while leaving unchanged the position of the cloud centre. We find that the heating rate decreases with α, and reduces to $0.5 \pm 0.3\,\mu\mathrm{K\,s^{-1}}$ for $\alpha = 0.3$. Although this dependence imposes some restrictions on the nature of the heating mechanism, further measurements are required to fully understand and possibly eliminate it.

A decisive advantage of the chip trap lies in the versatility of the lithographic wire structures. With the wire layout of Fig. 1, many more complicated potentials could be realized. As a first demonstration of these capabilities, we have created a condensate in configuration C2 and transported it over a distance of 1.6 mm along the chip surface using a 'magnetic conveyor belt'[6]. This is done by applying periodically modulated currents I_{M1} and I_{M2} with a relative phase shift of $\pi/2$. Figure 5a shows the cloud during transport over two conveyor periods; images were taken separately and then superposed. Figure 5b shows a series of time-of-flight images in 2.4-ms intervals after release at the final position: the expanding cloud shows the bimodal distribution of a BEC even after transport. This is encouraging for applications such as trapped-atom interferometry[23,24] with condensates. Because of this robustness, the simplicity of the set-up and the possibilities of chip-based potentials, we expect fruitful results from microchip BEC experiments in the near future. □

Received 27 July; accepted 11 September 2001.

1. Anderson, M. H., Ensher, J. R., Matthews, M. R., Wieman, C. E. & Cornell, E. A. Observation of Bose–Einstein condensation in a dilute atomic vapor. *Science* **269,** 198–201 (1995).
2. Davis, K. B. *et al.* Bose–Einstein condensation in a gas of sodium atoms. *Phys. Rev. Lett.* **75,** 3969–1690 (1995).
3. Bradley, C. C., Sackett, C. A. & Hulet, R. G. Bose–Einstein condensation of lithium: observation of limited condensate number. *Phys. Rev. Lett.* **78,** 985–989 (1997).
4. Barrett, M. D., Sauer, J. A. & Chapman, M. S. All-optical formation of an atomic Bose–Einstein condensate. *Phys. Rev. Lett.* **87,** 010404-1–010404-4 (2001).
5. Reichel, J., Hänsel, W. & Hänsch, T. W. Atomic micromanipulation with magnetic surface traps. *Phys. Rev. Lett.* **83,** 3398–3401 (1999).
6. Hänsel, W., Reichel, J., Hommelhoff, P. & Hänsch, T. W. Magnetic conveyer belt for transporting and merging trapped atom clouds. *Phys. Rev. Lett.* **86,** 608–611 (2001).
7. Calarco, T. *et al.* Quantum gates with neutral atoms: Controlling collisional interactions in time-dependent raps. *Phys. Rev. A* **61,** 022304-1–022304-11 (2000).
8. Weinstein, J. D. & Libbrecht, K. G. Microscopic magnetic traps for neutral atoms. *Phys. Rev. A* **52,** 4004–4009 (1995).
9. Ott, H., Fortagh, J., Schlotterbeck, G., Grossmann, A. & Zimmermann, C. Bose–Einstein condensation in a surface microtrap. *Phys. Rev. Lett.* (in the press).
10. Müller, D., Anderson, D. Z., Grow, R. J., Schwindt, P. D. D. & Cornell, E. A. Guiding neutral atoms around curves with lithographically patterned current-carrying wires. *Phys. Rev. Lett.* **83,** 5194–5197 (1999).
11. Dekker, N. H. *et al.* Guiding neutral atoms on a chip. *Phys. Rev. Lett.* **84,** 1124–1127 (2000).
12. Müller, D. *et al.* Waveguide atom beamsplitter for laser-cooled neutral atoms. *Opt. Lett.* **25,** 1382–1384 (2000).
13. Cassettari, D., Hessmo, B., Folman, R., Maier, T. & Schmiedmayer, J. Beam splitter for guided atoms. *Phys. Rev. Lett.* **85,** 5483–5487 (2000).
14. Reichel, J., Hänsel, W., Hommelhoff, P. & Hänsch, T. W. Applications of integrated magnetic microtraps. *Appl. Phys. B* **72,** 81–89 (2001).
15. Ketterle, W. & van Druten, N. J. in *Advances in Atomic, Molecular and Optical Physics* Vol. 37 (eds Bederson, B. & Walther, H.) 181–236 (Academic, San Diego, 1996).
16. Drndić, M., Johnson, K. S., Thywissen, J. H., Prentiss, M. & Westervelt, R. M. Micro-electromagnets for atom manipulation. *Appl. Phys. Lett.* **72,** 2906–2908 (1998).
17. Fortagh, J., Ott, H., Grossmann, A. & Zimmermann, C. Miniaturized magnetic guide for neutral atoms. *Appl. Phys. B* **70,** 701–708 (2000).
18. Anderson, B. P. & Kasevich, M. A. Loading a vapor-cell magneto-optic trap using light-induced atom desorption. *Phys. Rev. A* **63,** 023404-1–023404-4 (2001).
19. Petrov, D. S., Shlyapnikov, G. V. & Walraven, J. T. M. Phase-fluctuating 3D Bose–Einstein condensates in elongated traps. *Phys. Rev. Lett.* **87,** 050404-1–050404-4 (2001).
20. Dettmer, S. *et al.* Observation of phase fluctuations in Bose–Einstein condensates. *Phys. Rev. Lett.* (in the press); preprint cond-mat/0105525 at ⟨http://xxx.lanl.gov⟩ (2001).
21. Henkel, C., Pötting, S. & Wilkens, M. Loss and heating of particles in small and noisy traps. *Appl. Phys. B* **69,** 379–387 (1999).
22. Cornell, E. A., Ensher, J. R. & Wieman, C. E. in *Proc. Int. School of Physics "Enrico Fermi", Course CXL* (eds Inguscio, M., Stringari, S. & Wieman, C.) 15–66 (IOS, Amsterdam, 1999).
23. Hinds, E. A., Vale, C. J. & Boshier, M. G. Two-wire waveguide and interferometer for cold atoms. *Phys. Rev. Lett.* **86,** 1462–1465 (2001).
24. Hänsel, W., Reichel, J., Hommelhoff, P. & Hänsch, T. W. Trapped-atom interferometer in a magnetic microtrap. *Phys. Rev. A* (in the press).
25. Folman, R. *et al.* Controlling cold atoms using nanofabricated surfaces: Atom chips. *Phys. Rev. Lett.* **85,** 5483–5487 (2001).

Acknowledgements

This work was supported in part by the European Union under the IST programme (ACQUIRE project).

Correspondence and requests for materials should be addressed to J.R. (e-mail: jakob.reichel@physik.uni-muenchen.de).

Spatially resolved electronic structure inside and outside the vortex cores of a high-temperature superconductor

V. F. Mitrović*, E. E. Sigmund*, M. Eschrig†, H. N. Bachman*, W. P. Halperin*, A. P. Reyes‡, P. Kuhns‡ & W. G. Moulton‡

** Department of Physics and Astronomy, Northwestern University, Evanston, Illinois 60208, USA*
† Materials Science Division, Argonne National Laboratory, Argonne, Illinois 60439, USA
‡ National High Magnetic Field Laboratory, Tallahassee, Florida 32310, USA

Puzzling aspects of high-transition-temperature (high-T_c) superconductors include the prevalence of magnetism in the normal state and the persistence of superconductivity in high magnetic fields. Superconductivity and magnetism generally are thought to be incompatible, based on what is known about conventional superconductors. Recent results[1], however, indicate that antiferromagnetism can appear in the superconducting state of a high-T_c superconductor in the presence of an applied magnetic field. Magnetic fields penetrate a superconductor in the form of quantized flux lines, each of which represents a vortex of supercurrents. Superconductivity is suppressed in the core of the vortex and it has been suggested that antiferromagnetism might develop there[2]. Here we report the results of a high-field nuclear-magnetic-resonance (NMR) imaging experiment[3–5] in which we spatially resolve the electronic structure of near-optimally doped $YBa_2Cu_3O_{7-\delta}$ inside and outside vortex cores. Outside the cores, we find strong antiferromagnetic fluctuations, whereas